

Time-Resolved EPR Studies of Photogenerated Radical Ion Pairs Separated by *p*-Phenylene Oligomers and of Triplet States Resulting from Charge Recombination[†]

Zachary E. X. Dance, Qixi Mi, David W. McCamant, Michael J. Ahrens,
Mark A. Ratner,* and Michael R. Wasielewski*

Department of Chemistry and International Institute for Nanotechnology, Northwestern University,
Evanston, Illinois 60208-3113

Received: June 13, 2006; In Final Form: July 25, 2006

Photoexcitation of a series of donor–bridge–acceptor (D–B–A) systems, where D = phenothiazine (PTZ), B = *p*-phenylene (Ph_{*n*}), *n* = 1–5, and A = perylene-3,4:9,10-bis(dicarboximide) (PDI) results in rapid electron transfer to produce ¹(PTZ^{•+}–Ph_{*n*}–PDI^{•–}). Time-resolved EPR (TREPR) studies of the photogenerated radical pairs (RPs) show that above 150 K, when *n* = 2–5, the radical pair–intersystem crossing mechanism (RP–ISC) produces spin-correlated radical ion pairs having electron spin polarization patterns indicating that the spin–spin exchange interaction in the radical ion pair is positive, $2J > 0$, and is temperature dependent. This temperature dependence is most likely due to structural changes of the *p*-phenylene bridge. Charge recombination in the RPs generates PTZ–Ph_{*n*}–³PDI, which exhibits a spin-polarized signal similar to that observed in photosynthetic reaction-center proteins and some biomimetic systems. At temperatures below 150 K and/or at shorter donor–acceptor distances, e.g., when *n* = 1, PTZ–Ph_{*n*}–³PDI is also formed from a competitive spin–orbit–intersystem crossing (SO–ISC) mechanism that is a result of direct charge recombination: ¹(PTZ^{•+}–Ph_{*n*}–PDI^{•–}) → PTZ–Ph_{*n*}–³PDI. This SO–ISC mechanism requires the initial RP intermediate and depends strongly on the orientation of the molecular orbitals involved in the charge recombination as well as the magnitude of $2J$.

Introduction

Developing a fundamental understanding of energy, charge, and spin transport in chemical systems for solar energy conversion is important for sustainable energy utilization. A major challenge lies in finding molecules that exhibit long-distance charge transport mechanisms operating with the high efficiencies found in Nature.¹ In assembling electron donor–bridge–acceptor (D–B–A) systems optimized for the photoconversion of solar energy, the system must be designed to adopt the most efficient charge transport mechanism possible, one which maintains this efficiency as the bridge is lengthened.² The ability to achieve distance-independent, or “wirelike”, charge transport in artificial photosynthetic systems requires a thorough understanding of the three basic mechanisms involved in molecular nonresonant charge-transfer processes. The first is superexchange, where an electron or hole is transferred in a single step from donor to acceptor and the bridge is used as a medium for electronic coupling.^{3,4} In superexchange, the redox state of the bridge does not change, and the probability of transferring an electron/hole between donor and acceptor generally decreases exponentially with distance. The second mechanism is incoherent tunneling, where an electron or hole tunnels under successive energy barriers from one site to the next until it reaches a charge trap.^{5–7} The third mechanism is thermally activated hopping, where the energy barrier between sites is lowered by nuclear rearrangement to such an extent that the electron or hole surmounts the barrier.⁵ Because the length dependence of incoherent charge-transfer mechanisms is weak,

systems that utilize them are sometimes said to display molecular wirelike behavior.⁸ Most often, charge transfer within complex systems is due to some mixture of these three mechanisms,^{9–11} with the proportion of each determined by electronic energy level matching and electronic coupling, which are in turn determined primarily by bridge length, conformational rigidity, temperature, and the electronic properties of the redox centers.^{12–16}

In the superexchange mechanism, the bridge orbitals are energetically well-separated from those of the donor and acceptor, and the electronic coupling matrix element, V_{DA} , gives the effective interaction energy between the relevant orbitals on the donor and acceptor.^{17–19} Importantly, the rate of electron transfer is proportional to V_{DA}^2 , which is a strong function of D–B–A structure.^{20,21} Moreover, when the charge transport process originates from a state in which the redox centers are also paramagnetic, e.g., charge recombination from a radical ion pair (RP) state D^{•+}–B–A^{•–}, the superexchange coupling, V_{DA} , which dictates charge transfer, is the same coupling that determines the magnetic interaction between the unpaired spins in the RP. Therefore, the magnitude of the magnetic spin–spin exchange interaction, i.e., the singlet–triplet splitting between the two radicals, $2J$, and its dependence on molecular structure mirror that of V_{DA} .^{17–19,22–27} We have demonstrated earlier that $2J$ is proportional to V_{DA}^2 and is highly sensitive to both the RP distance and the structure of the intervening bridge system.^{14,15,28–32}

In this study, we use time-resolved EPR (TREPR) spectroscopy to explore the spin dynamics in a series of D–B–A molecules, which have been studied earlier using transient optical absorption spectroscopy and optically detected magnetic field effects (MFEs) on charge recombination.^{14,15} The D–B–A system consists of a series of *p*-phenylene (Ph_{*n*}) oligomers,

[†] Part of the special issue “Arthur J. Nozik Festschrift”.

* Corresponding authors. E-Mail: m-wasielewski@northwestern.edu (M.R.W.).

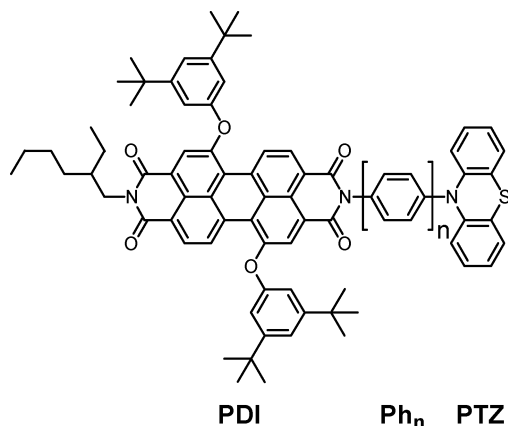


Figure 1. Chemical structure of PTZ-Ph_n-PDI, where $n = 1$ for compound **1**, $n = 2$ for compound **2**, etc.

where $n = 1-5$, that link a phenothiazine (PTZ) electron donor to a perylene-3,4,9,10-bis(dicarboximide) (PDI)³³ electron acceptor, Figure 1. Previous work has shown that selective photoexcitation of PDI within PTZ-Ph_n-PDI results in charge separation to produce a spin-coherent singlet radical ion pair (RP), $^1(\text{PTZ}^{+\bullet}-\text{Ph}_n-\text{PDI}^{-\bullet})$.^{14,15} The subsequent RP recombination dynamics depend on temperature and the magnitude of $2J$, both of which reflect structural changes within the RP.

Radical Pair-Intersystem Crossing and Triplet States from Charge Recombination. The mechanistic details of the radical pair-intersystem crossing mechanism (RP-ISC) and the theory behind magnetic field effects on electron transfer reactions have been researched extensively³⁴⁻³⁷ and have been applied to many donor-acceptor systems^{14,28,29,38-43} including biological systems.^{35,44-47} Following charge separation, an initially formed singlet RP will undergo electron-nuclear hyperfine coupling-induced RP-ISC to produce the triplet RP, $k_{\text{ST}}^{\text{RP}}$, Figure 2A, provided that the hyperfine interactions are comparable to or larger than $2J$ and the dipolar interaction (D) between the two radicals. Because the hyperfine interactions within each radical are usually small, this implies that $2J$ and D must be small as well. The subsequent charge recombination process is spin selective; i.e., the singlet RP $^1(\text{D}^{+\bullet}-\text{B}-\text{A}^{-\bullet})$ recombines to the singlet ground-state D-B-A with a rate constant $k_{\text{SS}}^{\text{CR}}$, while the triplet RP $^3(\text{D}^{+\bullet}-\text{B}-\text{A}^{-\bullet})$ recombines to yield the neutral local triplet $^3(\text{D}-\text{B}-\text{A})$ with a rate constant $k_{\text{TT}}^{\text{CR}}$. Application of a magnetic field results in Zeeman splitting of the RP triplet sublevels, which at low fields are best described by the zero-field eigenstates, T_X , T_Y , and T_Z that are quantized in the molecular framework, and at high fields are best described by the T_{+1} , T_0 , and T_{-1} eigenstates that are quantized along the applied magnetic field, Figure 2B. If $2J > 0$, the singlet energy level is above that of the triplet sublevels, Figure 2B, so that when the Zeeman energy from the applied field equals that of the singlet-triplet splitting, the highest-energy triplet sublevel crosses the singlet level and the RP-ISC rate is maximized. This mixing populates the triplet manifold, which, following spin-selective recombination, should produce a resonance in the triplet yield at B_{2J} , directly yielding $2J$.^{17,48} If $2J < 0$, the singlet energy level, S , is below that of the triplet sublevels, and the lowest-energy triplet sublevel crosses S , yielding the same information. The appearance of a distinct resonance depends critically on having a RP in which the two radicals have a relatively narrow distribution of distances and orientations between them, as in **1-5**, where there is a linear donor-acceptor geometry with donor-acceptor distances of 12.8, 17.1, 21.4, 25.7, and 30.0 Å, respectively. Consequently,

the observed resonances are extremely sensitive to small changes in molecular structure. We have previously used magnetic field effects (MFEs) on RP and triplet recombination product yields to measure the values of $2J$ for **2-5** at room temperature¹⁴ and the temperature dependence of $2J$ for **2-4**.¹⁵

The magnitude of $2J$ depends exponentially on the RP distance,

$$2J = 2J_0 e^{-\alpha(r-r_0)} \quad (1)$$

where r is the defined RP distance, α is a constant, and $2J_0$ is the value of spin-spin exchange interaction at r_0 , the minimum RP separation. In the high field limit at long RP distances, typically $\geq 15-20$ Å, population of the RP triplet state occurs exclusively by $S-T_0$ mixing, provided that $2J$ and D are small relative to the Zeeman splitting $g\beta\mathbf{B}$, where g is the electronic g -factor, β is the Bohr magneton, and \mathbf{B} is the applied magnetic field. At shorter RP distances, where $|2J|$ is large, two additional intersystem crossing mechanisms that also depend on the formation of the singlet radical pair precursor can operate. First, if $|2J| \sim g\beta\mathbf{B}$ and $|2J|$ is large enough so that $S-T_0$ mixing is inefficient, $S-T_{+1}$ ($2J > 0$) or $S-T_{-1}$ ($2J < 0$) mixing may occur. Second, if $|2J| \gg g\beta\mathbf{B}$, $S-T_0$, $S-T_{+1}$, and $S-T_{-1}$ mixing are all inefficient. Nevertheless, rapid intersystem crossing from the singlet radical pair may take place via a spin-orbit coupling mechanism to produce $^3(\text{D}-\text{B}-\text{A})$ directly by charge recombination, $k_{\text{ST}}^{\text{CR}}$, Figure 2A, provided that the symmetries of the orbitals involved in the electron transfer are such that the spin flip is accompanied by a significant change in orbital angular momentum.⁴⁹⁻⁵³ The first alternative mechanism will be discussed briefly later in this section, while the second mechanism will be discussed at length in the Discussion section.

Optically detected MFE measurements on reactant or product yields do not show how the spin polarization of the radicals within the RP evolves with time, how the structure of radicals may be changing, or how the dynamics of the medium couple with the spin dynamics of the RP. Fortunately, TREPR measurements can yield this information directly.⁵⁴⁻⁵⁶ If $2J$ and/or D are small, yet nonzero, $S-T_0$ mixing within $\text{D}^{+\bullet}-\text{B}-\text{A}^{-\bullet}$ will result in formation of so-called spin-correlated radical pair (SCRPs) states that can be identified through the unique polarization of the EPR transitions that occur between them.⁵⁷⁻⁶⁶ If $2J$ is larger, as may be the case when the $\text{D}^{+\bullet}-\text{B}-\text{A}^{-\bullet}$ distance is shorter, mixing of the S state of the radical pair with either T_{+1} ($2J > 0$) or T_{-1} ($2J < 0$) may also occur, which results in different polarization of the EPR transitions relative to those that result from $S-T_0$ mixing.⁶⁶

Without taking into account hyperfine interactions, the SCRPs spectrum consists of two antiphase doublets, centered at the g factors of the individual radicals that comprise the pair. The splitting in each doublet is determined by $2J$ and D . Resolved hyperfine interactions lead to further splitting of the doublet for each radical. The experimentally observed SCRPs spectrum is a superposition of the four-line spectra for all possible nuclear states of the RP, as well as all orientations with respect to the external magnetic field, \mathbf{B} . The positions (ω_{ij}) of the four EPR transitions for a SCRPs are⁵⁸⁻⁶⁰

$$\begin{aligned} \omega_{12} &= \omega_0 - \Omega - J + D_{\text{ZZ}}; \\ \omega_{34} &= \omega_0 - \Omega + J - D_{\text{ZZ}} \quad (2\text{a,b}) \end{aligned}$$

$$\begin{aligned} \omega_{13} &= \omega_0 + \Omega - J + D_{\text{ZZ}}; \\ \omega_{24} &= \omega_0 + \Omega + J - D_{\text{ZZ}} \quad (2\text{c,d}) \end{aligned}$$

where $\omega_0 = 1/2(\omega_{\text{PDI}} + \omega_{\text{PTZ}})$ is the center of the spectrum,

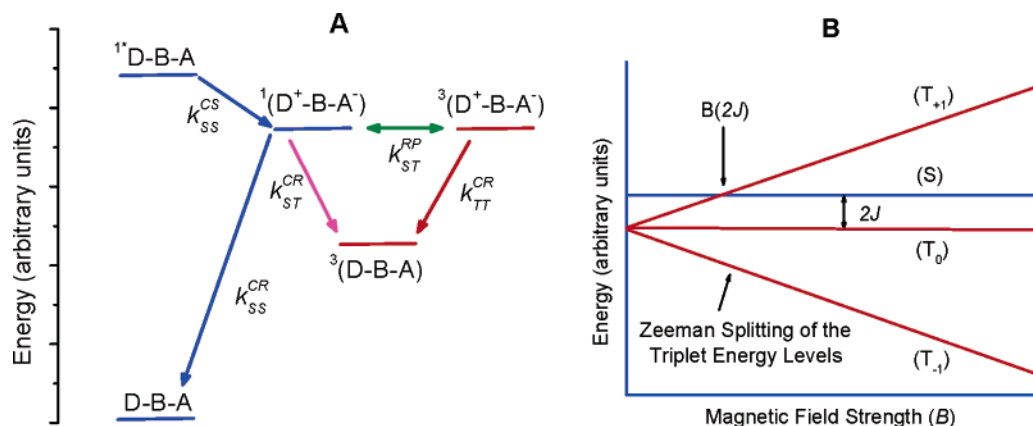


Figure 2. (A) Electron transfer and intersystem crossing pathways in a D-B-A system; (B) Radical ion pair energy levels as a function of magnetic field for $2J > 0$.

$$\Omega^2 = (J + D_{ZZ}/2)^2 + Q^2 \quad (3)$$

and

$$D_{ZZ} = D[3 \cos^2(\xi) - 1] \quad (4)$$

where ξ is the angle between the dipolar axis of the radical pair and the direction of the magnetic field \mathbf{B} . The mixing term Q between singlet and triplet states is

$$Q = \frac{1}{2}(g_1 - g_2)\beta\mathbf{B}/\hbar + \frac{1}{2}(\sum a_{1i}m_{1i} - \sum a_{2j}m_{2j}) \quad (5)$$

where g_1 and g_2 are the g factors of radicals 1 and 2, and a_{1i} and a_{2j} are the hyperfine coupling constants of radicals 1 and 2. The intensities of the transitions are

$$-I_{12} = -I_{13} = I_{24} = I_{34} = Q^2/(4\Omega^2) \quad (6)$$

The electron spin polarization (ESP) pattern of the EPR signal, i.e., which transitions are in enhanced absorption (A) or emission (E), is determined by the SCRIP sign rule,

$$\Gamma = \mu \cdot \text{sign}[J - D(3 \cos^2(\xi) - 1)] = (-) \text{ gives } E/A \text{ or } (+) \text{ gives } A/E \quad (7)$$

where μ is -1 or $+1$ for a singlet or triplet excited-state precursor, respectively. The model outlined above implicitly assumes that the decay rate constant from the singlet RP, k_{SS}^{CR} , is equal to the decay rate from the triplet RP, k_{TT}^{CR} , Figure 2A. However, the singlet and triplet RP generally recombine with different rates, i.e., $k_{SS}^{CR} \neq k_{TT}^{CR}$. Till and Hore³⁶ have extended the SCRIP model to describe a nondiffusing, exchange, and/or dipolar coupled radical pair in a strong static magnetic field incorporating the ability to assign different values to k_{SS}^{CR} and k_{TT}^{CR} .

The non-Boltzmann spin populations within the SCRIP are transferred to the neutral triplet state $3^*(D-B-A)$ that results from radical ion pair recombination within $3(D^+-B-A^-)$.^{54,67} The main features of the EPR spectrum of $3^*(D-B-A)$ arise from zero-field splitting (ZFS), which is a result of the magnetic dipole-dipole interaction between the two unpaired electrons in the triplet state. The Hamiltonian that describes this interaction is:⁶⁸⁻⁷¹

$$\mathcal{H}_{\text{dipolar}} = D(S_z^2 - S^2/3) + E(S_x^2 - S_y^2) \quad (8)$$

where D and E are the zero-field-splitting parameters and $S_{x,y,z}$ are the components of the total spin angular momentum operator

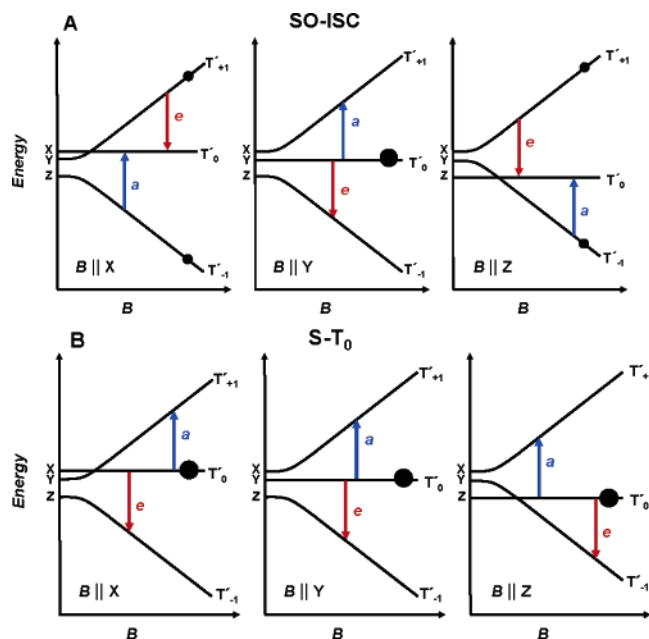


Figure 3. Energy levels of $3^*(D-B-A)$ formed by (A) SO-ISC with selective population of T'_Y ($D > 0$) and (B) S- T_0 mixing within a RP precursor. The arrows indicate the direction of the transition and are labeled a = enhanced absorption, e = emission.

(S) for the triplet state. The effect of this term is to lift the degeneracy of the triplet manifold in the absence of an external magnetic field as a function of the symmetry of the molecule. The polarization of the EPR transitions exhibited by $3^*(D-B-A)$ formed by a spin-orbit-inter-system crossing (SO-ISC) mechanism can be differentiated from the RP-ISC mechanism by the ESP pattern of the six EPR transitions, i.e., the two transitions at each canonical (x, y, z) orientation.⁶⁷ In SO-ISC, the three zero-field levels T'_X , T'_Y , and T'_Z of $3^*(D-B-A)$ are selectively populated, and this selectivity is carried over to the high-field energy levels. For example, assuming selective population of the T'_Y zero-field level and $D > 0$, Figure 3A shows that the six EPR transitions from low to high field yield an (e, a, e, a, e, a) polarization pattern, where a = enhanced absorption and e = emission. In contrast, RP-ISC acts directly on the high-field triplet sublevels of the RP via S- T_0 (or S- $T_{\pm 1}$) mixing, Figure 3B. Spin polarization is preserved upon recombination so that an (a, e, e, a, a, e) polarization pattern exhibited by $3^*(D-B-A)$ is the unique signature of the RP-ISC mechanism within D^+-B-A^- .

Experimental Section

The synthesis and characterization of compounds **1–5** have been reported previously.¹⁴ For TREPR, compounds **1–5** were purified by preparative TLC. Samples (~1 mM in toluene) were loaded in 4-mm OD × 2-mm ID quartz tubes and subjected to several freeze–pump–thaw degassing cycles on a vacuum line (10^{−4} Torr). The tubes were then sealed with a hydrogen torch. All samples were prepared in freshly distilled ACS-grade toluene.

TREPR measurements using continuous wave (CW) microwaves and direct detection were made using a Bruker Elexsys E580 X-band EPR spectrometer outfitted with a variable Q dielectric resonator (ER-4118X-MD5-W1). The temperature was controlled by an Oxford Instruments CF935 continuous flow cryostat using liquid He. Samples were photoexcited at 532 nm (1–2 mJ/pulse, 7 ns, 10 Hz) using the frequency-doubled output from a Nd:YAG laser (QuantaRay DCR-2). The polarization of the laser was set to 54.7° relative to the direction of the static magnetic field to avoid magnetophotoselection effects on the spectra. Following photoexcitation, kinetic traces of transient magnetization were accumulated under CW microwave irradiation (typically 6–20 mW). The field modulation was disabled to achieve a time response of $Q/\pi\nu \approx 40$ ns, where Q is the quality factor of the resonator and ν is the resonant frequency, while microwave signals in emission (e) and/or enhanced absorption (a) were detected in both the real and the imaginary channels (quadrature detection). Sweeping the magnetic field gave 2D complex spectra versus time and magnetic field. For each kinetic trace, the signal acquired prior to the laser pulse was subtracted from the data. Kinetic traces recorded at magnetic field values off-resonance were considered background signals, whose average was subtracted from all kinetic traces. The spectra were subsequently phased into a Lorentzian part and a dispersive part, and the former, also known as the imaginary magnetic susceptibility χ'' , is presented. Simulation of the powder-pattern spectra of the spin-polarized RP signals and the triplet states resulting from CR was performed using a home-written MATLAB program⁷² following published procedures.^{70,73}

Ground-state absorption measurements were made on a Shimadzu UV-1601 spectrophotometer. The optical density of all samples was maintained between 0.8 and 1.5 at 532 nm ($\epsilon_{\text{PDI},532\text{ nm}} = 30500\text{ M}^{-1}\text{ cm}^{-1}$) at room temperature.¹⁴ Time-resolved fluorescence data were collected using a home-built cavity-dumped Ti:sapphire oscillator⁷⁴ coupled to a streak camera detection system (Hamamatsu C4334 Streakscope). The laser produced 24-μJ pulses at 791 nm with an 820 kHz repetition rate and ~30-fs pulse duration. The laser pulses were frequency doubled in a nonlinear crystal (0.3 mm BBO) to produce 395.5 nm excitation pulses that were attenuated with a half-wave plate and polarizer to 60–600 pJ/pulse before the sample. Synchronization between the laser pulse train and the streak camera was provided by the acousto-optic cavity dumper (NEOS N13389, N64389-SYN) and a photodiode–discriminator combination that detected the intracavity repetition rate of the laser (82 MHz). The illumination and collection optics were in a standard 90° geometry with the polarization of the excitation pulses and the detected fluorescence controlled by broadband polarizers.⁷⁵ The anisotropy, r , was calculated according to:

$$r = \frac{I_{\parallel} - I_{\perp}}{I_{\parallel} + 2I_{\perp}} = \frac{I_{\text{VV}} - CI_{\text{VH}}}{I_{\text{HV}} + 2CI_{\text{VH}}} \quad (9)$$

where I_{VV} (I_{VH}) is the time-dependent intensity of the vertically

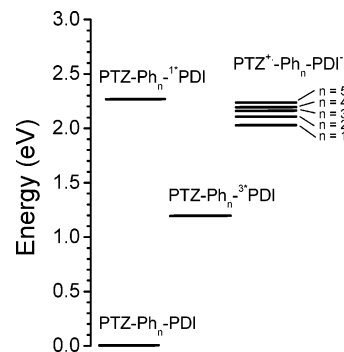


Figure 4. Energy levels for the electronic states relevant to the electron-transfer pathways for **1–5**.

(horizontally) polarized emission excited with vertically polarized light, and C is the relative sensitivity of the detection system to vertically and horizontally polarized emission.⁷⁵ C is calculated using the unpolarized emission that occurs with horizontal excitation: $C = I_{\text{HV}}/I_{\text{HH}}$. Fluorescence lifetimes and anisotropy decay times were determined by nonlinear least-squares fitting including deconvolution of the instrument response of the streak camera (0.043 ns for a 2-ns time window, and 0.40 ns for a 20-ns time window). Room-temperature measurements were performed on dilute samples ($A_{547} < 0.08$) in a 10-mm cuvette. Low-temperature measurements were performed in a cryostat (see below) with front-face illumination of the concentrated sample of **5** ($A_{547} = 1.0$, $A_{391} = 0.19$). The concentrated sample was chosen in order to reproduce the conditions of the EPR and low-temperature absorption samples. At room temperature, the concentrated sample of **5** in the cryostat cell exhibited identical kinetics to the dilute sample in the cuvette.

For variable temperature UV–vis and time-resolved fluorescence experiments, a liquid-nitrogen-cooled optical dewar (Janis Research VPS-100) was utilized. Each sample was loaded into a sealed optical cell with ~2–3-mm path length constructed from two transparent quartz windows and a Viton O-ring spacer. The sample holder was seated in the dewar, which was then evacuated to ~10^{−5} Torr. Sample temperature was maintained to within ±0.5 K by a Lake Shore Cryotronics model DRC-82C temperature controller.¹⁵ The sample was allowed to equilibrate for 30 min at each temperature prior to photolysis.

Results

Radical Pair TREPR Spectra. Femtosecond transient absorption experiments have shown that photoexcitation of PDI in **1–5** produces ¹*PDI exclusively, followed by rapid, nonadiabatic electron transfer from PTZ to ¹*PDI to give ¹(PTZ⁺–Ph_{1–5}–PDI[−]).¹⁴ The approximate energy levels for the relevant electronic states are given in Figure 4.¹⁴ Following photoexcitation, spin-polarized RP signals were observed for both **4** and **5**, Figure 5, while a very weak signal was observed for **3** only at low temperatures (shown in Figure 6C), and no signals were observed for **1** or **2**. The RP spectra of **4** and **5** were simulated with the SCR mechanism using the model of Till and Hore.³⁶ The best fits to the data are given in Figure 5, while the fitting parameters are summarized in Table 1. Because of the weak nature and poor signal-to-noise ratio of the RP signal from **3**, no attempt was made to simulate it, while the fits for **4** are only approximate due to the same limitations. The measured g factors and hyperfine coupling constants of PDI^{•−} (ref 76) and PTZ^{•+} (ref 77) were used in the simulations. These quantities were assumed to be temperature independent. Following from eq 7, $2J$ is positive for the RPs in both **4** and **5**, given that

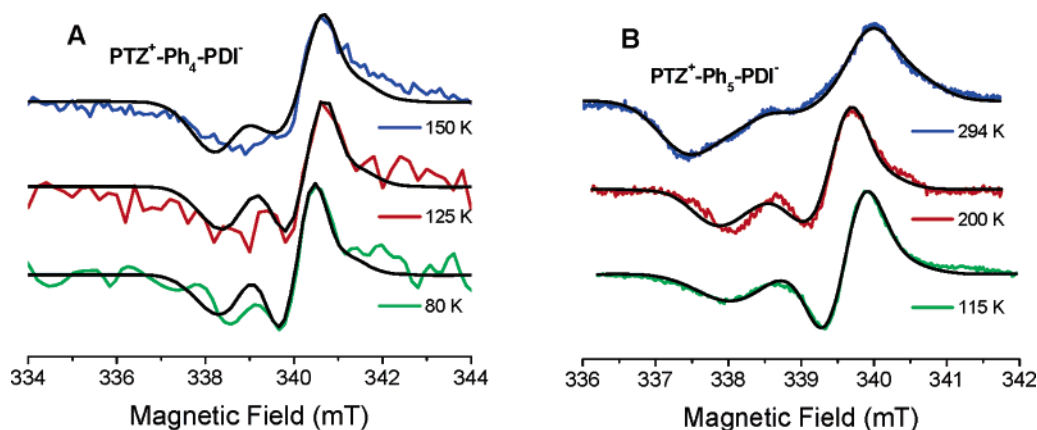


Figure 5. TREPR spectra of (A) $\text{PTZ}^+-\text{Ph}_4-\text{PDI}^-$ and (B) $\text{PTZ}^+-\text{Ph}_5-\text{PDI}^-$ at 100 ns following a 532 nm, 1.5 mJ laser pulse at the indicated temperatures in toluene. Smooth curves superimposed on the experimental spectra are computer simulations of the radical pair spectra (see text) with the parameters given in Table 1. Positive features are in enhanced absorption, while negative features are in emission.

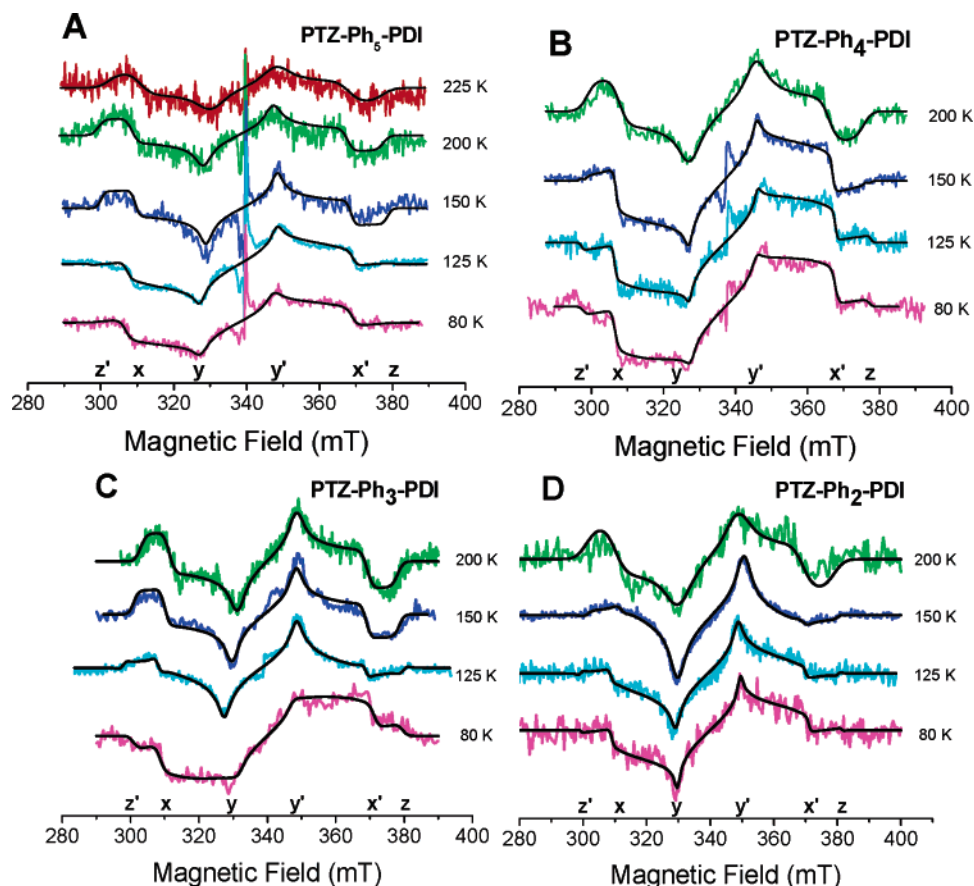


Figure 6. TREPR spectra of (A) **5**, (B) **4**, (C) **3**, and (D) **2** in toluene at the indicated temperatures at 200 ns following a 532 nm, 1.5 mJ laser pulse. The sharp features at the center of the spectra in (A) and (B) are the radical pair signals, while the broad features are $\text{PTZ}-\text{Ph}_n-^3\text{PDI}$. The canonical orientations of each transition are indicated. Smooth curves superimposed on the experimental spectra are computer simulations of the triplet with the parameters given in Table 2.

TABLE 1: RP Simulation Parameters for 4 and 5 at 100 ns after the Laser Pulse

compound	<i>T</i> (K)	2 <i>J</i> (mT)	$k_{\text{SS}}^{\text{CR}}$ (s^{-1})	$k_{\text{TT}}^{\text{CR}}$ (s^{-1})
4	150	0.9 ± 0.3	$9 \pm 1 \times 10^6$	$3 \pm 0.1 \times 10^7$
4	125	0.8 ± 0.3	$1 \pm 0.1 \times 10^7$	$2 \pm 0.1 \times 10^7$
4	80	0.7 ± 0.3	$1 \pm 0.1 \times 10^7$	$2 \pm 0.1 \times 10^7$
5	294	1.0 ± 0.05	$3.5 \pm 0.5 \times 10^6$	$2.7 \pm 0.5 \times 10^7$
5	200	0.52 ± 0.05	$4.2 \pm 0.5 \times 10^6$	$2.5 \pm 0.5 \times 10^7$
5	115	0.42 ± 0.05	$1.2 \pm 0.5 \times 10^7$	$1.6 \pm 0.5 \times 10^7$

photoexcitation of PDI initially produces a singlet RP (ref 14) and that the experimentally determined absolute phases of the RP spectra are E/A .^{78,79} The dipolar interaction between the

electron spins in both **4** and **5** is ≤ 0.3 mT due to the long RP distances.⁶⁶ Experimental details of the absolute phase determination can be found in the Supporting Information.

TREPR Spectra of Triplet States Resulting from Charge Recombination. The TREPR spectra of **5** exhibit two major features at all temperatures: a broad triplet spectrum with a width of ~ 76 mT, having an electron spin polarization (ESP) phase pattern that changes as a function of temperature, Figure 6A, and the narrow RP spectrum at $g \sim 2$, which was discussed above, superimposed on the triplet spectrum. The broad triplet spectrum is detectable at temperatures ranging from 80 K to as high as 225 K, at which toluene is an isotropic liquid. The ESP

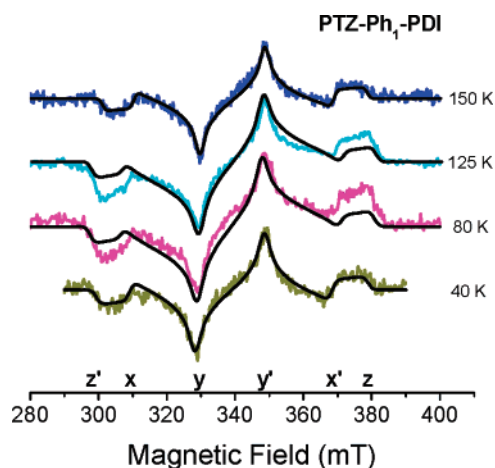


Figure 7. TREPR spectra of PTZ-Ph₁-³*PDI in toluene at the indicated temperatures at 200 ns following a 532 nm, 1.5 mJ laser pulse. The canonical orientations of each transition are indicated. Smooth curves superimposed on the experimental spectra are computer simulations of the triplet with the parameters given in Table 2.

phase pattern is (*a*, *e*, *e*, *a*, *a*, *e*) above 125 K, but changes gradually to (*e*, *e*, *a*, *a*, *a*, *a*) below 125 K due to the onset of a competitive SO-ISC mechanism.

The TREPR spectra of 2–4 show characteristics that are similar to those of 5, Figure 6B–D, i.e., a broad triplet spectrum is present over a large temperature range. The triplet ESP phase patterns for 2–4 also exhibit temperature dependencies analogous to that of 5. The narrow spectrum resulting from the RP is only observed in 4 at lower temperatures, is barely visible for 3 at lower temperatures, and is absent for 1 and 2 at all temperatures. The TREPR spectra of 1, Figure 7, are very different from those of 2–5. The broad triplet spectrum is only present below the melting point of toluene (~160 K). The (*e*, *a*, *e*, *a*, *e*, *a*) ESP pattern is indicative of a SO-ISC mechanism and remains constant at all temperatures at which the spectrum is observed.

The parameters from the line shape analysis of the broad triplet spectra are summarized in Table 2. All spectra in 2–5 were simulated using a linear combination of RP-ISC and SO-ISC mechanisms. The spectra of 3–5 exhibit ESP phase patterns that are primarily a result of the S-T₀ RP-ISC mechanism at 150 K and above. However, as the temperature decreases, the ESP pattern changes, with the simulations indicating that a SO-ISC mechanism is the main source of ³*PDI at lower temperatures. The spectra of 2 are similar to 3–5, but the temperature at which the SO-ISC mechanism becomes the principal source of ³*PDI occurs between 150 and 200 K. The ³*PDI signal from 1 is simulated using the SO-ISC mechanism exclusively (no contribution from RP-ISC), and the relative population rates heavily favor the T'_γ spin state relative to T'_x or T'_z states. The fits are in good agreement with experimental results at 150 and 40 K. However, at 125 and 80 K, the simulations deviate from experimental results for the outermost transitions, Figure 7.

Temperature-Dependent UV-Vis Spectroscopy. The ground-state UV-vis spectra of compounds 1–5 at room temperature have an absorption band at 550 nm due to PDI with a lower intensity vibronic band at 515 nm. Additionally, there is a feature between 300 and 350 nm from Ph_n that red-shifts and grows in intensity relative to the PDI peaks as *n* increases.¹⁴ Temperature-dependent UV-vis spectra of 3, Figure 8, and 5 (not shown) reveal that, as the temperature is lowered from room temperature to 184 K, there is an enhancement of the 515 nm peak relative to the 550 nm peak. Previous work

TABLE 2: Zero-Field Splitting Parameters and Relative Population Rates of the Zero-Field Spin States Obtained from Simulations of the Triplet-State TREPR Spectra of 1–5

<i>T</i> (K)	<i>D</i> (mT) ^a	<i>E</i> (mT) ^a	<i>A'</i> _x ^b	<i>A'</i> _y ^b	<i>A'</i> _z ^b	<i>c</i> _{RP} ^c	<i>c</i> _{SO} ^c
Compound 5							
225	37.62	−6.57				1.0	
200	39.17	−6.65				1.0	
150	39.36	−6.62				1.0	
115	41.65	−6.88	0.86	1	0	0.31	0.69
80	41.16	−7.11	1	0.91	0	0.40	0.60
Compound 4							
200	38.39	−6.64				1.0	
150	39.37	−6.88	1	0.76	0	0.57	0.43
125	40.19	−7.10	1	0.81	0.005	0.25	0.75
80	39.69	−7.21	1	0.73	0	0.24	0.76
Compound 3							
200	37.60	−6.78				1.0	
150	39.48	−6.70	0.13	1	0.45	0.96	0.04
125	40.81	−6.88	0.69	1	0	0.40	0.60
80	39.87	−7.70	1	0.82	0	0.04	0.96
Compound 2							
200	39.02	−6.77				1.0	
150	39.16	−6.07	0	1	0.15	0.46	0.54
125	40.45	−6.96	0.49	1	0	0.40	0.60
80	40.97	−7.09	0.77	1	0	0.29	0.71
Compound 1							
150	38.78	−6.59	0.11	1	0		1
125	41.62	−7.56	0.35	1	0		1
80	41.62	−7.56	0.35	1	0		1
40	39.82	−6.50	0.10	1	0		1

^a *D* and *E* parameters obtained using eq 8 to fit experimental results.

^b Relative population rates for spin-orbit-inter-system crossing (SO-ISC). ^c Coefficient preceding S-T₀ contribution and SO-ISC contribution to the overall fit using the functional form: *c*_{RP} * (S-T₀) + *c*_{SO} * (SO-ISC).

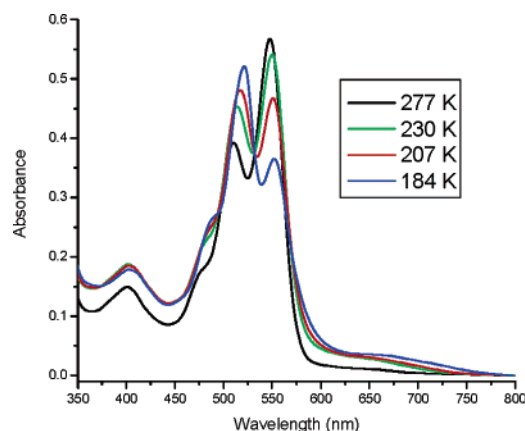


Figure 8. Optical absorption spectra of PTZ-Ph₃-PDI in toluene at the indicated temperatures.

has shown that a fully covalent, cofacial PDI₂ reference dimer displays a very similar enhancement of the 515 nm band at the expense of the 550 nm band.^{33,80–82} The increasing intensity of the 515 band as the temperature is lowered suggests that the PDI acceptors in these D-B-A molecules aggregate in a parallel, π -stacked geometry. In fact, some aggregation of the PDI chromophores is apparent at temperatures as high as 230 K.

Time-Resolved Fluorescence Anisotropy. The time-resolved fluorescence results are summarized in Table 3. Because the emission transition dipole lies along the long axis of the PDI molecule, the anisotropies are expected to decay to zero according to a simple exponential model:

TABLE 3: Rotational Correlation Times as Deduced by Time Resolved Fluorescence

molecule	<i>T</i> (K)	<i>V</i> (Å ³) ^a	<i>η</i> (cP) ^b	<i>θ_R</i> (ns)
PDI	298	981	0.56	0.40 ± 0.03
3	298	1410	0.56	0.56 ± 0.03
5	298	1770	0.56	0.71 ± 0.06
5	230	1770	1.73	1 ± 0.6 (40%) 9 ± 9 (60%)
5	207	1770	3.60	8 ± 2
5	184	1770	11.0	12 ± 4

^a Molecular volumes are calculated for an ellipsoidal molecule with elliptical radii of 2.5 and 7.5 Å with overall length increasing from 25 to 36 to 45 Å for the PDI monomer to **3** to **5** series. ^b Viscosities were calculated according to Assael et al.⁸³ and Barlow et al.⁸⁴

$$r(t) = r(0) e^{-t/\theta_R} \quad (10)$$

where θ_R is the axial rotational correlation time.⁷⁵ In the limit of “stick” diffusion of an ellipsoidal molecule, we can determine the rotational correlation time with

$$\theta_R = \frac{V\eta}{kT} f(a, b, c) \quad (11)$$

where *V* is the volume of the molecule, *η* is the solvent viscosity, *a*, *b*, and *c* are the ellipsoidal radii of the molecule, and the function, *f*(*a*, *b*, *c*), subsumes all the shape dependence of the correlation time. The initial fluorescence anisotropies, *r*(0), of between −0.1 and −0.05 were all significantly less than the expected value of −0.2 for a chromophore whose absorption transition dipole is perpendicular to the emission transition dipole, as is the case for 395.5 nm excitation of PDI into its *S*₂ state. This is most likely due to a change in the relative angle between the *S*₁ and *S*₂ transition dipoles from 90° to between 60 and 66° in this highly substituted perylene.⁷⁵ At room temperature, θ_R changes linearly with estimated molecular volume, increasing from 0.40 ns in the PDI monomer, to 0.56 ns in **3**, and finally, to 0.71 ns in **5**, Table 3.

Discussion

Radical Pair TREPR Spectra. An examination of the parameters used to simulate the RP TREPR spectra of **4** and **5**, Table 1, shows that *2J* decreases as the temperature decreases. This is readily seen in the spectra as well (Figure 5), which narrow as the temperature decreases. We showed earlier that *2J* for **2–4** determined from MFEs on the yield of ³*PDI following RP recombination decreases as the temperature decreases; for example, *2J* for **4** decreases from 8.3 mT at 345 K to 4.7 mT at 218 K.¹⁵ It should be noted that values of *2J* estimated from MFE resonances due to *S*–*T*_{±1} level-crossings and those determined directly from TREPR data may differ somewhat due to the fact that the energies of the level crossings can depend on the nuclear spin states.⁸⁵ Given the error bars on the data for **4** in Figure 5A, the small changes of *2J* with temperature should be viewed with appropriate caution. However, the value of *2J* obtained for **5** at 294 K agrees well with that measured earlier using MFEs and displays a similar decrease with decreasing temperature. Equations 3 and 6 show that the intensity of the SCR signal is inversely proportional to *2J*, so that the SCR signal intensity should increase for these systems as the temperature decreases. The result is that *2J* becomes small enough in **4** and to some degree in **3** for the SCR signal to become detectable at low temperatures, but remains too large for detection at room temperature or at shorter RP distances. The inability to observe intense RP signals for **1–3** and for **4** at

higher temperatures given the shorter RP distances and/or larger *2J* values for these molecules is consistent with this picture.

The decrease in *2J* with decreasing temperature is most likely due to a reduction in the amplitude of torsional motions about the single bonds joining the phenyls of the bridge. This results in relaxation of the system into conformations in which the dihedral angles between the *π*-systems of the phenyls are larger, which diminishes the electronic coupling between them. The fact that aggregation of **1–5** occurs as the temperature is lowered may also affect the RP properties. We have shown that *π*-stacking of PDI molecules can result in electron hopping between the PDIs on the time scale of their hyperfine couplings.⁷⁶ Additional electron delocalization in the RP due to *π*-stacking of two or more PDI molecules may result in smaller values of *2J*. Although aggregation may contribute to the observed decrease in *2J* as the temperature is lowered, this effect cannot be distinguished easily from the decrease that is expected from torsional motions between the Ph groups of the bridge molecules.

It is notable that $k_{\text{TT}}^{\text{CR}} > k_{\text{SS}}^{\text{CR}}$ for both **4** and **5** as determined from the simulations of their RP spectra over the range of temperatures measured, Table 1. This agrees with our results obtained earlier using MFE measurements on the RP and triplet recombination yields of **4** and **5** (as well as **2** and **3**) at low magnetic field strengths. We have shown previously that the total reorganization energy, *λ*, for charge recombination of the RPs within these molecules at room temperature is about 0.6 eV.¹⁴ Spin-selective formation of the ground state by charge recombination from the singlet RPs of **4** and **5**, where $\Delta G k_{\text{SS}}^{\text{CR}} = -2.1$ to -2.2 eV, lies deep within the Marcus inverted region⁸⁶ of the rate vs free energy profile, while the formation of the corresponding local triplet state from the triplet RPs, where $\Delta G k_{\text{TT}}^{\text{CR}} = -0.9$ to -1.0 eV, is much closer to the peak of the rate vs free energy profile. Thus, energy gap considerations alone predict that $k_{\text{TT}}^{\text{CR}}$ should be larger than $k_{\text{SS}}^{\text{CR}}$. Both $k_{\text{SS}}^{\text{CR}}$ and $k_{\text{TT}}^{\text{CR}}$ change by less than a factor of 3 over the entire range of temperatures measured. These small changes, which are just outside the error bars on the data, cannot easily be attributed to a single source. For example, over this large temperature range, $\Delta G k_{\text{SS}}^{\text{CR}}$, $\Delta G k_{\text{TT}}^{\text{CR}}$, *λ*, undoubtedly change. In addition, the electronic coupling matrix elements for charge recombination also change, as indicated by the fact that *2J* is temperature dependent.

Triplet-State TREPR Spectra Resulting from RP–ISC. The fluorescence quantum yield of PDI is approximately unity,⁸⁷ so that the yield of ³*PDI produced directly from the photoexcited singlet state, ¹*PDI, via SO–ISC is insignificant. In fact, triplet EPR spectra have not been observed for any monomeric PDI derivatives following direct photoexcitation. The formation of *π*-stacked *H*-aggregates of chromophores sometimes leads to enhanced intersystem crossing;⁸⁸ however, we have examined model covalent, cofacial PDI dimers,⁸⁹ and have found that photoexcitation produces singlet excimer-like states predominantly. Thus, the observation of reasonably intense triplet EPR spectra in **1–5** following charge separation in these molecules must be due to mechanisms of ³*PDI formation that depend in some way on the formation of a RP. A variety of ESP patterns are observed in the triplet-state spectra of **1–5**, which depend on both the length of the *p*-phenylene oligomer and the temperature. These patterns provide insights into the triplet formation mechanisms that occur in these molecules.

The ESP pattern (*a*, *e*, *e*, *a*, *a*, *e*) of the triplet spectra of PTZ–Ph_{3–5}–³*PDI at and above 150 K and of PTZ–Ph₂–³*PDI at 200 K uniquely results from RP–ISC, where an intermediate

RP, i.e., $\text{PTZ}^{+\bullet}-\text{Ph}_n-\text{PDI}^{\bullet-}$, is required for its realization.⁶⁷ In such cases, population of $\text{PTZ}-\text{Ph}_{2-5}-^3\text{PDI}$ following charge recombination is selective with respect to the high-field eigenfunctions and not the molecular zero-field eigenfunctions as is the case for SO–ISC. The high-field T'_0 triplet sublevel is overpopulated at all canonical orientations, and the ESP patterns are preserved within a particular transition, i.e., $T'_0 \leftrightarrow T'_1$ or $T'_0 \leftrightarrow T'_{-1}$, Figure 3B.^{90–92} The observed (*a*, *e*, *e*, *a*, *a*, *e*) ESP pattern seen at higher temperatures in **2–5** requires that the triplet zero-field splitting parameter $D > 0$. Although this same ESP pattern can be formed if $D < 0$ and selective overpopulation of $T'_{\pm 1}$ occurs, the latter is unlikely given that $|2J| \ll g\beta B$ for **2–5** at the temperatures at which ^3PDI is observed. The triplet spectra of $\text{PTZ}-\text{Ph}_{2-5}-^3\text{PDI}$ above 150 K and $\text{PTZ}-\text{Ph}_2-^3\text{PDI}$ at 200 K in toluene can be accurately simulated with the RP–ISC mechanism, making the primary contribution to the line shape relative to the SO–ISC mechanism, Table 2. The origin of ^3PDI produced by a SO–ISC mechanism will be discussed in detail below.

An unusual aspect of these systems is the existence of a spin-polarized EPR signal for ^3PDI in the *liquid phase*. Generally, in the liquid phase, the anisotropic magnetic dipole–dipole interaction averages to zero and no triplet spectrum is observed.^{93,94} If, however, molecular reorientation is not rapid enough to cause the dipolar contribution to vanish, then a triplet spectrum may be seen. Recently, Yamauchi et al.^{94,95} suggested that the conditions necessary to observe triplet spectra in fluid solution involve a delicate balance of several parameters, including relatively small ZFS parameters and significant chemically induced dynamic electron polarization (CIDEP). The size of the molecule, and consequently its rotational correlation time, were also found to play an important role in the observation of the triplet spectrum.

The UV–vis absorption spectra of **1–5** indicate that these molecules aggregate in toluene at temperatures of 230 K and below, Figure 8. We have demonstrated that similar UV–vis spectra occur in covalent, cofacial PDI dimers in which the transition dipoles for the lowest energy transitions in each of the two PDI chromophores, which lie along the *N–N* axis, are constrained to a parallel orientation.³³ Recent work by Myers-Kelley has modeled the blue-shifted λ_{max} and distorted Franck–Condon progression in related systems, where exciton coupling is treated explicitly for all vibronic levels of the electronic transitions.⁸² Unfortunately, the spectra do not indicate the size of the aggregates, nor do they preclude the possibility that any two PDI molecules within the aggregates may deviate somewhat from a strictly cofacial orientation relative to one another to minimize steric interactions.

Because the rotational correlation time for a system is a function of both molecular size and the viscosity of the solvent at a given temperature, it is reasonable to expect aggregates to have longer rotational correlation times than their monomeric constituents. Given that the rate constants for charge separation within **3** and **5** are $6.2 \times 10^8 \text{ s}^{-1}$ and $1.3 \times 10^8 \text{ s}^{-1}$, respectively, at 294 K,¹⁴ and the fluorescence lifetime of ^1PDI is intrinsically 4.5 ns, the fluorescence emission of **3** and **5** in toluene is sufficiently long-lived, so that time-resolved fluorescence anisotropy experiments were used to measure their rotational correlation times. Data for **5** were obtained as a function of temperature down to a range at which some of the TREPR data is obtained, Table 3. The rotational correlation time depends on the molecular volume, eq 11, so that the larger size of an aggregate should be reflected in an increase in the fluorescence anisotropy decay time, eq 10. At 230 K, the anisotropy exhibits

a biexponential decay with a fast decay of ~ 1 ns, probably due to the monomer, and a longer ~ 9 ns decay, most likely due to an aggregated species. The accuracy of the low-temperature anisotropies is hampered by the relatively large standard deviations in the data due to the inherent difficulty of measuring ~ 12 ns anisotropy decays for a molecule with a shorter fluorescence lifetime. The anisotropy of **5** decays with single-exponential kinetics at 207 K with a time constant of ~ 8 ns, and then increases to ~ 12 ns at 184 K. Presumably, at these lower temperatures, the long monoexponential anisotropy decay is due largely to the aggregate. The low-temperature rotational correlation times are shorter than expected for an aggregated species given the potential for significant changes in V , η , and T in eq 11; however, the large error bars associated with these measurements preclude a full discussion of the significance and quantification of the rotational correlation times. In purely qualitative terms, rotational correlation times of ~ 10 ns are significantly slower than the inverse of the frequency (~ 1 ns) that corresponds to the energy of the dipolar interaction D in the triplet states of these molecules. Thus, the triplet TREPR spectra observed in liquid toluene are a result of slowed molecular reorientation to the point where the dipolar interaction is no longer averaged out. Although aggregation occurs, the D and E values of $\text{PTZ}-\text{Ph}_{2-5}-^3\text{PDI}$ do not change significantly as the temperature decreases either within one system or in one system relative to another. Thus, it is unlikely that the triplet excitation in $\text{PTZ}-\text{Ph}_{2-5}-^3\text{PDI}$ is either delocalized or hopping between PDI molecules within the aggregates at frequencies that are comparable to or faster than those that correspond to D (~ 1 GHz).

Triplet-State TREPR Spectra Resulting from SO–ISC.

As either the RP distance or the temperature decreases, the fraction of the triplet-state TREPR spectrum due to the RP–ISC mechanism diminishes, while that due to a SO–ISC mechanism increases, Table 1. Given that direct $^1\text{PDI} \rightarrow ^3\text{PDI}$ by SO–ISC is negligible, RP formation is most likely responsible for SO–ISC leading to $\text{PTZ}-\text{Ph}_{1-5}-^3\text{PDI}$. If the orientation between the relevant orbitals of D and A is such that rapid electron transfer between them results in a significant change in orbital angular momentum, recombination of $^1(\text{D}^{+\bullet}-\text{B}-\text{A}^{\bullet-})$ may be accompanied by a spin flip to directly yield $^3(\text{D}-\text{B}-\text{A})$.^{49,51,52} In this case the spin–orbit interaction does not result in $^1(\text{D}^{+\bullet}-\text{B}-\text{A}^{\bullet-}) \rightarrow ^3(\text{D}^{+\bullet}-\text{B}-\text{A}^{\bullet-})$ because $\langle ^1(\text{D}^{+\bullet}-\text{B}-\text{A}^{\bullet-}) | \mathcal{H}_{\text{SO}} | ^3(\text{D}^{+\bullet}-\text{B}-\text{A}^{\bullet-}) \rangle = 0$ due to the fact that there is no change in the spatial orbital for this process.⁹⁶ Okada et al.⁴⁹ originally proposed this mechanism to explain the formation of a pyrene triplet state within 30 ps following photoexcitation of pyrene to its lowest excited singlet state in a covalently linked pyrene-*N*-methylaniline derivative. The rapid rate of pyrene triplet-state formation precluded the RP–ISC mechanism, which typically occurs on a time scale of a few nanoseconds. They found that the ISC rate was strongly dependent upon the mutual orientation of the donor and acceptor groups and concluded that $\langle ^1(\text{D}^{+\bullet}-\text{B}-\text{A}^{\bullet-}) | \mathcal{H}_{\text{SO}} | ^3(\text{D}-\text{B}-\text{A}) \rangle$ is increased when the electron donating and accepting molecular orbitals are approximately perpendicular to each other. This mechanism is formally similar to rapid SO–ISC that occurs in an $n-\pi^*$ electronic transition within a single chromophore.

Wasielewski et al.⁵⁰ studied a zinc porphyrin electron donor to which a tetracyano-naphthoquinodimethane acceptor was rigidly attached so that the π systems of the donor and acceptor were oriented approximately 60° relative to one another. Photoexcitation of this system at 10 K results in quantitative electron transfer from the porphyrin to the acceptor with $\tau =$

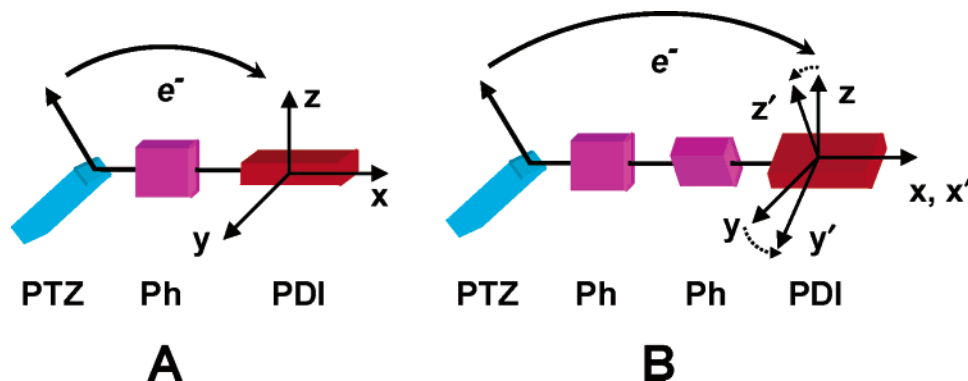


Figure 9. (A) Electron transfer from PTZ to ^1PDI in PTZ-Ph₁-PDI between orbitals oriented in the x - z plane results in an angular momentum change along y . (B) Rotation of the PDI π system away from the x - z plane in PTZ-Ph₂₋₅-PDI due to changes in the Ph-Ph torsional angles results in an angular momentum change in both the x and y directions. These angular momentum changes result in SO-ISC to the corresponding spin sublevels of ^3PDI .

2.2 ps to produce a radical ion pair that recombines in about 0.5 ns to give a high yield of the zinc porphyrin triplet state having a TREPR spectrum with an ESP pattern indicative of SO-ISC to the in-plane sublevels of the zinc porphyrin. In contrast, photoexcitation of the zinc porphyrin in the absence of the acceptor produces a porphyrin triplet state in which the out-of-plane sublevel is populated exclusively. Similarly, van Willigen et al.⁵¹ used TREPR to provide convincing evidence that this same mechanism is operative in 10-methylacridinium systems having arene electron donors attached to their 9 position. The ZFS parameters were found to remain essentially constant, whereas the ESP phase pattern was a sensitive function of the orientation of the donor and acceptor ring systems. Their analysis also indicated that, similar to the analysis of Okada et al.,⁴⁹ an approximately perpendicular orientation of the donor and acceptor enhanced the rate of SO-ISC. This was reflected in the triplet EPR spectra as an orientation-dependent spin selectivity of the population rates A'_x , A'_y , and A'_z . In a more recent example, Gould et al.⁵² analyzed rapid intersystem crossing in a series of exciplexes between cyanoanthracene acceptors and alkylbenzene donors and concluded that rapid SO-ISC results in direct population of the excited cyanoanthracene triplet from the singlet exciplex.

In addition to the dependence on orientation between the orbitals relevant to charge transfer, the magnitude of the electronic coupling between D and A strongly influences the contribution from the SO-ISC process.^{50,52,53,97-99} The value of $2J$ for the RP in **1** is at least 800 mT, as estimated from an extrapolation of a linear plot of $\ln(|2J|)$ vs r_{DA} obtained from the measured MFEs for **2-5**,¹⁴ so that $|2J| \gg g\beta B$ for **1** and the yield of ^3PDI resulting from RP-ISC approaches zero because the large energy gap between singlet and triplet RP states prohibits significant mixing. The TREPR spectrum of ^3PDI in **1** is not observed in fluid solution. This is a consequence of the fact that **1** is the smallest molecule of the series and most likely has the fastest rotational correlation time in liquid toluene. However, an intense ^3PDI spectrum is observed for **1** at temperatures ≤ 150 K, Figure 7. Simulations of the ^3PDI TREPR spectra of **1** agree well with the experimental results at 150 and 40 K, however at 125 and 80 K, the simulations deviate somewhat from experimental results for the outermost transitions. It is likely that anisotropic spin lattice relaxation is the cause of the deviations, and further modeling is needed to clarify this result.

In aromatic molecules such as PDI, the triplet axis system usually coincides with the lowest electronic transitions and is clearly dictated by the molecular structure.^{97,100,101} Although we

have not assigned the principal triplet molecular axes of ^3PDI experimentally, it is reasonable to assume that the z -axis is the out-of-plane axis, as is typical of π - π^* triplets of aromatic molecules, which leaves the x and y axes in the plane of ^3PDI .¹⁰²⁻¹⁰⁴ In our simulations, the central zero-field sublevel is assigned to T'_y , Figure 3A, and the observed (e, a, e, a, e, a) ESP pattern for **1** is indicative of a SO-ISC mechanism with selective population of T'_y for $D > 0$.^{92,105}

Density functional theory (DFT) calculations using the B3LYP functional and 6-31G** basis set show that the nitrogen atom of PTZ is essentially tetrahedral and the dihedral angle between the nitrogen lone pair orbital of PTZ and the π system of the attached Ph in the energy-minimized structure of **1** is 89° , while that between PDI and Ph is 74° .¹⁴ Thus, electron transfer from PTZ to ^1PDI involves moving an electron between two orbitals having a geometry change in the x - z plane as defined in Figure 9. Using the right-hand rule, this implies that the angular momentum change is along the y direction, so that the spin-orbit interaction that drives $^1(\text{PTZ}^{+\bullet}-\text{Ph}_1-\text{PDI}^{-\bullet}) \rightarrow \text{PTZ}-\text{Ph}_1-^3\text{PDI}$ should selectively populate T'_y of PTZ-Ph₁- ^3PDI , as is observed in the TREPR spectra of the triplet state of **1**.^{106,107} An additional contribution to spin-orbit coupling may arise from the presence of the sulfur atom in PTZ cation, i.e., the heavy atom effect.^{53,108} However, because calculations indicate that the unpaired spin density at this position is low, it is unlikely that this contribution will be a significant source of intersystem crossing.

At temperatures above 150 K, the ESP phase pattern in PTZ-Ph₂₋₅- ^3PDI is primarily the result of S- T_0 mixing resulting from RP-ISC, but at 125 K and below, the ESP phase pattern for **2-5** changes to (e, e, e, a, a, a), Figure 6. Simulations of the PTZ-Ph₂₋₅- ^3PDI TREPR spectra at low temperatures using a linear combination of the RP-ISC mechanism in addition to a SO-ISC mechanism with approximately equal population of the zero-field T'_x and T'_y eigenstates agrees well with experiment (see Figure 6A, 80 K, and Table 2). This observation can be explained by reference again to Figure 9. The Ph-Ph torsional angles in **2-5** are all about 40° in the neutral bridge molecule and diminish to about 25° if the bridge is oxidized.¹⁴ These torsional angles result in a change in the dihedral angle between the PDI π -system and the nitrogen lone pair orbital of PTZ, so that angular momentum changes occur in both the x and y directions following electron transfer. Because spin-orbit coupling matrix elements are inherently symmetry dependent,^{97,98,107} these components result in selective population of both T'_x and T'_y for **2-5**, which produces the observed (e, e, e, a, a, a) ESP pattern seen at 125 K and below

in the TREPR spectra. The increase in the fraction of PTZ–Ph_{2–5}–³PDI produced by direct charge recombination from the singlet RP (k_{ST}^{CR} , Figure 2A) as the temperature decreases is most likely due to a decrease in the amplitudes of the torsional motions about Ph–Ph single bonds. This results from the large increase in toluene viscosity as the temperature is lowered,^{83,109} especially in the glassy state below 160 K.⁸⁴ A narrow distribution of large Ph–Ph dihedral angles will promote SO–ISC by the mechanism indicated in Figure 9.

Conclusions

TREPR studies show that the spin dynamics of both photo-generated RPs and the neutral local triplet states that result from RP charge recombination are a strong function of both RP distance and temperature in the PTZ–Ph_n–PDI series, where $n = 1–5$. Above 150 K, when $n = 1$, the RP lifetime is too short to observe by TREPR. In addition, $|2J| \gg g\beta B$, so that the RP–ISC cannot occur. In contrast, above 150 K, when $n = 2–5$, the lifetimes of the RPs are sufficiently long and $|2J| \ll g\beta B$, so that RP–ISC via S–T₀ mixing occurs, which produces a spin-correlated radical pair. Charge recombination leads to PTZ–Ph_{2–5}–³PDI, which exhibit the unique ESP pattern seen in the photosynthetic reaction center that is the signature of the RP–ISC mechanism. Aggregation of PTZ–Ph_n–PDI molecules below 230 K combined with increasing solvent viscosity slows molecular reorientation and allows EPR detection of PTZ–Ph_n–³PDI in liquid solution. Below 150 K, when $n = 1–5$, a rapid SO–ISC mechanism where $^1(PTZ^{+•}-Ph_{1–5}-PDI^{-•}) \rightarrow PTZ-Ph_{1–5}-^3PDI$ competes with RP–ISC. This SO–ISC mechanism is characterized by the ESP phase patterns of the PTZ–Ph_{1–5}–³PDI TREPR spectra, and depends on the relative orientation of the orbitals involved in the charge recombination as well as the magnitude of the electronic coupling between the donor and acceptor, mirrored by $2J$. These results reveal the considerable level of structurally dependent mechanistic complexity responsible for charge and spin transport within conjugated oligomers, and provide insights into how their structures may be controlled to enhance their properties of interest to solar energy conversion.

Acknowledgment. This work was supported by the Division of Chemical Sciences, Office of Basic Energy Sciences, U.S. Department of Energy under grant no. DE-FG02-99ER-14999 (M.R.W.). M.A.R. acknowledges support from the DARPA MolApps program and the NSF Chemistry Division. The authors wish to thank Randall H. Goldsmith (NU), Dr. Michael J. Tauber (NU), and Dr. Ralph Weber (Bruker, Inc.) for helpful discussions.

Supporting Information Available: Experimental details regarding the determination of the radical pair EPR signal phase. This material is available free of charge via the Internet at <http://pubs.acs.org>.

References and Notes

- (1) Parson, W. W.; Scherz, A.; Warshel, A. *Springer Ser. Chem. Phys.* **1985**, 42, 122–130.
- (2) Jortner, J.; Ratner, M. A. *Molecular Electronics*; Blackwell: London, 1997.
- (3) Bixon, M.; Jortner, J. *Adv. Chem. Phys.* **1999**, 106, 35–202.
- (4) Jortner, J.; Bixon, M.; Langenbacher, T.; Michel-Beyerle, M. E. *Proc. Natl. Acad. Sci. U.S.A.* **1998**, 95, 12759–12765.
- (5) Berlin, Y. A.; Burin, A. L.; Ratner, M. A. *Chem. Phys.* **2002**, 275, 61–74.
- (6) Berlin, Y. A.; Burin, A. L.; Ratner, M. A. *J. Phys. Chem. A* **2000**, 104, 443–445.
- (7) Berlin, Y. A.; Hutchison, G. R.; Rempala, P.; Ratner, M. A.; Michl, J. *J. Phys. Chem. A* **2003**, 107, 3970–3980.
- (8) Troisi, A.; Ratner, M. A. *Mol. Nanoelectron.* **2003**, 1–18.
- (9) Segal, D.; Nitzan, A.; Davis, W. B.; Wasielewski, M. R.; Ratner, M. A. *J. Phys. Chem. B* **2000**, 104, 3817–3829.
- (10) Segal, D.; Nitzan, A.; Ratner, M. A.; Davis, W. B. *J. Phys. Chem. B* **2000**, 104, 2790–2793.
- (11) Paulson, B. P.; Miller, J. R.; Gan, W.-X.; Closs, G. L. *J. Am. Chem. Soc.* **2005**, 127, 4860–4868.
- (12) De la Torre, G.; Giacalone, F.; Segura, J. L.; Martin, N.; Guldi, D. M. *Chem.–Eur. J.* **2005**, 11, 1267–1280.
- (13) Giacalone, F.; Segura, J. L.; Martin, N.; Guldi, D. M. *J. Am. Chem. Soc.* **2004**, 126, 5340–5341.
- (14) Weiss, E. A.; Ahrens, M. J.; Sinks, L. E.; Gusev, A. V.; Ratner, M. A.; Wasielewski, M. R. *J. Am. Chem. Soc.* **2004**, 126, 5577–5584.
- (15) Weiss, E. A.; Tauber, M. J.; Kelley, R. F.; Ahrens, M. J.; Ratner, M. A.; Wasielewski, M. R. *J. Am. Chem. Soc.* **2005**, 127, 11842–11850.
- (16) Weiss, E. A.; Tauber, M. J.; Ratner, M. A.; Wasielewski, M. R. *J. Am. Chem. Soc.* **2005**, 127, 6052–6061.
- (17) Anderson, P. W. *Phys. Rev.* **1959**, 115, 2–13.
- (18) Anderson, P. W. *Phys. Rev.* **1950**, 79, 350–356.
- (19) Kramers, H. A. *Physica* **1934**, 1, 182–192.
- (20) Marcus, R. A. *J. Chem. Phys.* **1965**, 43, 679–701.
- (21) Jortner, J. *J. Chem. Phys.* **1976**, 64, 4860–4867.
- (22) Kobori, Y.; Sekiguchi, S.; Akiyama, K.; Tero-Kubota, S. *J. Phys. Chem. A* **1999**, 103, 5416–5424.
- (23) Paddon-Row, M. N.; Shephard, M. J. *J. Phys. Chem. A* **2002**, 106, 2935–2944.
- (24) Volk, M.; Haberle, T.; Feick, R.; Ogorodnik, A.; Michel-Beyerle, M. E. *J. Phys. Chem.* **1993**, 97, 9831–9836.
- (25) Closs, G. L.; Miller, J. R. *Science* **1988**, 240, 440–447.
- (26) Yamashita, J.; Kondo, J. *Phys. Rev.* **1958**, 109, 730–741.
- (27) Feher, G.; Okamura, M. In *Tunneling Conference*; Chance, B., Devault, D., Frauenfelder, H., Marcus, R. A., Schreiffer, J. R., Sutin, N., Eds.; Academic Press: New York, 1979; pp 729–743.
- (28) Lukas, A. S.; Bushard, P. J.; Weiss, E. A.; Wasielewski, M. R. *J. Am. Chem. Soc.* **2003**, 125, 3921–3930.
- (29) Weiss, E. A.; Ratner, M. A.; Wasielewski, M. R. *J. Phys. Chem. A* **2003**, 107, 3639–3647.
- (30) Weiss, E. A.; Sinks, L. E.; Lukas, A. S.; Chernick, E. T.; Ratner, M. A.; Wasielewski, M. R. *J. Phys. Chem. B* **2004**, 108, 10309–10316.
- (31) Goldsmith, R. H.; Sinks, L. E.; Kelley, R. F.; Betzen, L. J.; Liu, W. H.; Weiss, E. A.; Ratner, M. A.; Wasielewski, M. R. *Proc. Natl. Acad. Sci. U.S.A.* **2005**, 102, 3540–3545.
- (32) Weiss, E. A.; Tauber, M. J.; Ratner, M. A.; Wasielewski, M. R. *J. Am. Chem. Soc.* **2005**, 127, 6052–6061.
- (33) van der Boom, T.; Hayes, R. T.; Zhao, Y.; Bushard, P. J.; Weiss, E. A.; Wasielewski, M. R. *J. Am. Chem. Soc.* **2002**, 124, 9582–9590.
- (34) Weller, A.; Staerk, H.; Treichel, R. *Faraday Discuss. Chem. Soc.* **1984**, 78, 271–278.
- (35) Hoff, A. J.; Gast, P.; van der Vos, R.; Franken, E. M.; Lous, E. J. *Z. Phys. Chem.* **1993**, 180, 175–192.
- (36) Till, U.; Hore, P. J. *Mol. Phys.* **1997**, 90, 289–296.
- (37) Steiner, U. E.; Ulrich, T. *Chem. Rev.* **1989**, 89, 51–147.
- (38) Schulten, K.; Staerk, H.; Weller, A.; Werner, H.-J.; Nickel, B. Z. *Phys. Chem.* **1976**, 101, 371–390.
- (39) Tanimoto, Y.; Okada, N.; Itoh, M.; Iwai, K.; Sugiyama, K.; Takemura, F.; Nakagaki, R.; Nagakura, S. *Chem. Phys. Lett.* **1987**, 136, 42–46.
- (40) Sakaguchi, Y.; Hayashi, H. *J. Phys. Chem. A* **1997**, 101, 549–555.
- (41) Werner, U.; Kuhnle, W.; Staerk, H. *J. Phys. Chem.* **1993**, 97, 9280–9287.
- (42) Tadjikov, B.; Smirnov, S. *Phys. Chem. Chem. Phys.* **2001**, 3, 204–212.
- (43) Tsentlovich, Y. P.; Morozova, O. B.; Avdievich, N. I.; Ananchenko, G. S.; Yurkovskaya, A. V.; Ball, J. D.; Forbes, M. D. E. *J. Phys. Chem. A* **1997**, 101, 8809–8816.
- (44) Blankenship, R. E.; Schaafsma, T. J.; Parson, W. W. *Biochim. Biophys. Acta* **1977**, 461, 297–305.
- (45) Plato, M.; Moebius, K.; Michel-Beyerle, M. E.; Bixon, M.; Jortner, J. *J. Am. Chem. Soc.* **1988**, 110, 7279–7285.
- (46) Werner, H.-J.; Schulten, K.; Weller, A. *Biochim. Biophys. Acta* **1978**, 502, 255–268.
- (47) Norris, J. R.; Bowman, M. K.; Budil, D. E.; Tang, J.; Wraight, C. A.; Closs, G. L. *Proc. Natl. Acad. Sci. U.S.A.* **1982**, 79, 5532–5536.
- (48) Shultz, D. A.; Fico, R. M., Jr.; Bodnar, S. H.; Kumar, R. K.; Vostrikova, K. E.; Kampf, J. W.; Boyle, P. D. *J. Am. Chem. Soc.* **2003**, 125, 11761–11771.
- (49) Okada, T.; Karaki, I.; Matsuzawa, E.; Mataga, N.; Sakata, Y.; Misumi, S. *J. Phys. Chem.* **1981**, 85, 3957–3960.
- (50) Wasielewski, M. R.; Johnson, D. G.; Svec, W. A.; Kersey, K. M.; Minsek, D. W. *J. Am. Chem. Soc.* **1988**, 110, 7219–7221.

- (51) van Willigen, H.; Jones, G., II.; Farahat, M. S. *J. Phys. Chem.* **1996**, *100*, 3312–3316.
- (52) Gould, I. R.; Boiani, J. A.; Gaillard, E. B.; Goodman, J. L.; Farid, S. *J. Phys. Chem. A* **2003**, *107*, 3515–3524.
- (53) Khudyakov, I. V.; Serebrennikov, Y. A.; Turro, N. J. *Chem. Rev.* **1993**, *93*, 537–570.
- (54) Levanon, H.; Hasharoni, K. *Prog. React. Kinet.* **1995**, *20*, 309–346.
- (55) Schweiger, A.; Jeschke, G. *Principles of Pulsed Electron Paramagnetic Resonance*; Oxford University Press: New York, 2001.
- (56) Hore, P. J. In *Advanced EPR in Biology and Biochemistry*; Hoff, A. J., Ed.; Elsevier: Amsterdam, 1989; pp 405–440.
- (57) Hore, P. J.; Hunter, D. A.; McKie, C. D.; Hoff, A. J. *Chem. Phys. Lett.* **1987**, *137*, 495–500.
- (58) Closs, G. L.; Forbes, M. D. E.; Norris, J. R. *J. Phys. Chem.* **1987**, *91*, 3592–3599.
- (59) Hore, P. J. *Analysis of Polarized EPR Spectra*; Elsevier: Amsterdam, 1989.
- (60) Norris, J. R.; Morris, A. L.; Thurnauer, M. C.; Tang, J. J. *Chem. Phys.* **1990**, *92*, 4239–4249.
- (61) Hasharoni, K.; Levanon, H.; Gersdorff, J. v.; Kurreck, H.; Möbius, K. *J. Chem. Phys.* **1993**, *98*, 2916–2926.
- (62) Hasharoni, K.; Levanon, H.; Greenfield, S. R.; Gosztola, D. J.; Svec, W. A.; Wasielewski, M. R. *J. Am. Chem. Soc.* **1995**, *117*, 8055–8056.
- (63) Hasharoni, K.; Levanon, H.; Greenfield, S. R.; Gosztola, D. J.; Svec, W. A.; Wasielewski, M. R. *J. Am. Chem. Soc.* **1996**, *118*, 10228–10235.
- (64) Carbonera, D.; DiValentin, M.; Corvaja, C.; Agostini, G.; Giacometti, G.; Liddell, P. A.; Kuciauskas, D.; Moore, A. L.; Moore, T. A.; Gust, D. J. *Am. Chem. Soc.* **1998**, *120*, 4398–4405.
- (65) Levanon, H.; Galili, T.; Regev, A.; Wiederricht, G. P.; Svec, W. A.; Wasielewski, M. R. *J. Am. Chem. Soc.* **1998**, *120*, 6366–6373.
- (66) Shaakov, S.; Galili, T.; Stavitski, E.; Levanon, H.; Lukas, A.; Wasielewski, M. R. *J. Am. Chem. Soc.* **2003**, *125*, 6563–6572.
- (67) Levanon, H.; Norris, J. R. *Chem. Rev.* **1978**, *78*, 185–198.
- (68) Hutchinson, C. A.; Mangum, B. W. *J. Chem. Phys.* **1958**, *29*, 952–953.
- (69) Hutchinson, C. A.; Mangum, B. W. *J. Chem. Phys.* **1961**, *34*, 908–922.
- (70) Wasserman, E.; Snyder, L. C.; Yager, W. A. *J. Chem. Phys.* **1964**, *41*, 1763–1772.
- (71) Blank, A.; Levanon, H. *Concepts Magn. Reson., Part A* **2005**, *25*, 18–39.
- (72) *MATLAB*; The MathWorks, Inc.: Natick, MA, 2006.
- (73) Kottis, P.; Lefebvre, R. *J. Chem. Phys.* **1963**, *39*, 393–403.
- (74) Pshenichnikov, M. S.; de Boerij, W. P.; Wiersma, D. A. *Opt. Lett.* **1994**, *19*, 572–575.
- (75) Lakowicz, J. R. *Principles of Fluorescence Spectroscopy*; Kluwer: Dordrecht, 1999.
- (76) Tauber, M. J.; Giaimo, J. M.; Kelley, R. F.; Rybtchinski, B.; Wasielewski, M. R. *J. Am. Chem. Soc.* **2006**, *128*, 1782–1783.
- (77) Clarke, D.; Gilbert, B. C.; Hanson, P. J. *Chem. Soc., Perkin Trans. 2* **1976**, 114–124.
- (78) Adrian, F. J. *J. Chem. Phys.* **1972**, *57*, 5107–5113.
- (79) Atherton, N. M. In *Principles of Electron Spin Resonance*; Horwood, E., Ed.; Ellis Horwood Limited: Chichester, West Sussex, U.K. 1993.
- (80) Ahrens, M. J.; Sinks, L. E.; Rybtchinski, B.; Liu, W.; Jones, B. A.; Giaimo, J. M.; Gusev, A. V.; Goshe, A. J.; Tiede, D. M.; Wasielewski, M. R. *J. Am. Chem. Soc.* **2004**, *126*, 8284–8294.
- (81) Giaimo, J. M.; Gusev, A. V.; Wasielewski, M. R. *J. Am. Chem. Soc.* **2002**, *124*, 8530–8531.
- (82) Myers-Kelley, A. J. *Chem. Phys.* **2003**, *119*, 3320–3331.
- (83) Assael, M. J.; Dalaouti, N. K.; Dymond, J. H. *Int. J. Thermophys.* **2000**, *21*, 291–299.
- (84) Barlow, A. J.; Lamb, J.; Matheson, A. J. *Proc. R. Soc. London, Ser. A* **1966**, *292*, 322–342.
- (85) Hayashi, H. *Introduction to Dynamic Spin Chemistry: Magnetic Field Effects upon Chemical and Biochemical Reactions*; World Scientific: Singapore, 2004, p 78.
- (86) Marcus, R. A. *J. Chem. Phys.* **1956**, *24*, 966–978.
- (87) Ford, W. E.; Kamat, P. V. *J. Phys. Chem.* **1987**, *91*, 6373–6380.
- (88) Kasha, M.; Rawles, H. R.; El-Bayoumi, M. L. *Pure Appl. Chem.* **1965**, *11*, 371–392.
- (89) Ahrens, M. J.; Sinks, L. E.; Rybtchinski, B.; Liu, W.; Jones, B. A.; Giaimo, J. M.; Gusev, A. V.; Goshe, A. J.; Tiede, D. M.; Wasielewski, M. R. *J. Am. Chem. Soc.* **2004**, *126*, 8284–8294.
- (90) Dutton, P. L.; Leigh, J. S.; Reed, D. W. *Biochim. Biophys. Acta* **1973**, *292*, 654–664.
- (91) Dutton, P. L.; Leigh, J. S.; Seibert, M. *Biochem. Biophys. Res. Commun.* **1972**, *46*, 406–413.
- (92) Thurnauer, M. C. *Rev. Chem. Intermed.* **1979**, *3*, 197–230.
- (93) Weissman, S. I. *Acc. Chem. Res.* **1973**, *6*, 233–238.
- (94) Yamauchi, S. *Bull. Chem. Soc. Jpn.* **2004**, *77*, 1255–1268.
- (95) Yamauchi, S.; Takahashi, A.; Iwasaki, Y.; Unno, M.; Ohba, Y.; Higuchi, J.; Blank, A.; Levanon, H. *J. Phys. Chem. A* **2003**, *107*, 1478–1485.
- (96) Lim, B. T.; Okajima, S.; Chandra, A. K.; Lim, E. C. *Chem. Phys. Lett.* **1981**, *79*, 22–27.
- (97) El-Sayed, M. A. *J. Chem. Phys.* **1974**, *60*, 4502–4507.
- (98) Salem, L.; Rowland, C. *Angew. Chem., Int. Ed. Engl.* **1972**, *11*, 92–111.
- (99) Morais, J.; Hung, R. R.; Grabowski, J. J.; Zimmt, M. B. *J. Phys. Chem.* **1993**, *97*, 13138–13144.
- (100) Siegel, S.; Goldstein, L. J. *J. Chem. Phys.* **1965**, *43*, 4185–4187.
- (101) Siegel, S.; Judeikis, H. S. *J. Phys. Chem.* **1966**, *70*, 2205–2211.
- (102) Hutchinson, C. A. In *The Triplet State*; Zahlan, A. B., Ed.; University Press: Cambridge, 1967; pp 63–100.
- (103) Thurnauer, M. C.; Norris, J. R. *Chem. Phys. Lett.* **1977**, *47*, 100–105.
- (104) Siegel, S.; Judeikis, H. S. *J. Phys. Chem.* **1966**, *70*, 2201–2204.
- (105) Thurnauer, M. C.; Katz, J. J.; Norris, J. R. *Proc. Natl. Acad. Sci. U.S.A.* **1975**, *72*, 3270–3274.
- (106) van der Waals, J. H.; de Groot, M. S. In *The Triplet State*; Zahlan, A. B., Ed.; University Press: Cambridge, 1967; pp 101–132.
- (107) El-Sayed, M. A. In *Excited States*; Lim, E. C., Ed.; Academic Press: New York, 1974; Vol. 1, pp 35–77.
- (108) Katsuki, A.; Kobori, Y.; Tero-Kubota, S.; Milikisyants, S.; Paul, H.; Steiner, U. E. *Mol. Phys.* **2002**, *100*, 1245–1259.
- (109) Santos, F. J. V.; Nieto de Castro, C. A.; Dymond, J. H.; Dalaouti, N. K.; Assael, M. J.; Nagashima, A. *J. Phys. Chem. Ref. Data* **2006**, *35*, 1–8.